Journal of Computational Physics 509 (2024) 113037

Contents lists available at ScienceDirect

Journal of Computational Physics

journal homepage: www.elsevier.com/locate/jcp

Efficient energy stable numerical schemes for Cahn–Hilliard equations with dynamical boundary conditions

Xinyu Liu [a], Jie Shen [b], Nan Zheng [c,*]

[a] Department of Mathematics, Purdue University, West Lafayette, IN 47907, USA
[b] School of Mathematical Science, Eastern Institute of Technology, Ningbo, China
[c] Department of Applied Mathematics, The Hong Kong Polytechnic University, Hung Hom, Kowloon, Hong Kong

ARTICLE INFO

Keywords:
Cahn-Hilliard equation
Dynamic boundary conditions
Scalar auxiliary variable
Gradient flow
Spectral methods
Energy stability

ABSTRACT

In this paper, we propose a unified framework for studying the Cahn–Hilliard equation with two distinct types of dynamic boundary conditions, namely, the Allen–Cahn and Cahn–Hilliard types. Using this unified framework, we develop a linear, second-order, and energy-stable scheme based on the multiple scalar auxiliary variables (MSAV) approach. We design efficient and decoupling algorithms for solving the corresponding linear system in which the unknown variables are intricately coupled both in the bulk and at the boundary. Several numerical experiments are shown to validate the proposed scheme, and to investigate the effect of different dynamical boundary conditions on the dynamics of phase evolution under different scenarios.

1. Introduction

The Cahn–Hilliard equation was originally introduced in [1] to model phase separation processes of binary mixtures, which can be written as follows

$$\phi_t = \nabla \cdot (\mathbb{M}(\phi)\nabla\mu), \quad t > 0, \ \boldsymbol{x} \in \Omega, \tag{1.1a}$$

$$\mu = -\epsilon\Delta\phi + \frac{1}{\epsilon}F'(\phi), \quad t > 0, \boldsymbol{x} \in \Omega. \tag{1.1b}$$

In the equations, ϕ is a phase function with a thin, smooth transitional layer, whose thickness is proportional to the parameter ϵ, $\mathbb{M}(\phi) \geq 0$ is the mobility function; μ is the so called chemical potential, which can be expressed as the variational derivative of the energy functional

$$E_{\text{bulk}}(\phi) = \int_\Omega \frac{\epsilon}{2}|\nabla\phi|^2 + \frac{1}{\epsilon}F(\phi)d\boldsymbol{x}, \tag{1.2}$$

where ϵ is an interface thickness parameter, and F is usually either the thermodynamically relevant logarithmic potential function [1]

$$F(y) = -\frac{1}{2}kT_c y^2 + \frac{1}{2}kT[(1-y)\log(1-y) + (1+y)\log(1+y)], \ y \in \mathbb{R}, \tag{1.3}$$

* Corresponding author.
E-mail addresses: liu1957@purdue.edu (X. Liu), jshen@eitech.edu.cn (J. Shen), znan2017@163.com (N. Zheng).

https://doi.org/10.1016/j.jcp.2024.113037
Received 3 March 2023; Received in revised form 22 March 2024; Accepted 18 April 2024

Available online 24 April 2024

with k being the Boltzmann's constant and $0 < T < T_c$, or its approximation in the double-well form (cf. [2–5])

$$F(y) = \frac{1}{4}(y^2 - 1)^2, \ y \in \mathbb{R}. \tag{1.4}$$

When the interfaces do not touch the boundary, we can prescribe the homogeneous Neumann boundary conditions

$$\partial_{\boldsymbol{n}}\mu|_{\partial\Omega} = 0, \quad \partial_{\boldsymbol{n}}\phi|_{\partial\Omega} = 0, \tag{1.5}$$

where $\boldsymbol{n}$ is the outward normal of $\partial\Omega$. Then, we derive from (1.1)-(1.5) the conservation of mass in the bulk:

$$\int_\Omega \phi(t)d\boldsymbol{x} = \int_\Omega \phi(0)d\boldsymbol{x}, \tag{1.6}$$

and the energy dissipation law:

$$\frac{d}{dt}E_{\text{bulk}}(\phi) = -\int_\Omega |\mathbb{M}(\phi)\nabla\mu|^2 d\boldsymbol{x}. \tag{1.7}$$

However, when the interface touches the boundary, it becomes a moving contact line problem (cf. [6,7] and the references therein), so $\partial_{\boldsymbol{n}}\mu|_{\partial\Omega} = 0$ in (1.5) is no longer valid. Various dynamic boundary conditions have been proposed (see [8–11] and the references therein). In particular, the authors in [10,8] proposed to use

$$\phi_t = -\mu_\Gamma, \qquad t > 0, \ \boldsymbol{x} \in \Gamma, \tag{1.8a}$$

$$\mu_\Gamma = -\delta\Delta_\Gamma\phi + \lambda\phi + \frac{1}{\delta}G'(\phi) + \epsilon\partial_{\boldsymbol{n}}\phi, \qquad t > 0, \ \boldsymbol{x} \in \Gamma, \tag{1.8b}$$

where μ_Γ is the boundary chemical potential which is independent of the trace of μ on Γ, δ is related to surface diffusion on Γ, λ is a non-negative constant, $G(\phi)$ is a surface potential function which usually takes the double well form, Δ_Γ is the Laplace-Beltrami operator on the boundary Γ and $\partial_{\boldsymbol{n}}$ is the normal derivative at the boundary. In particular, the dynamic boundary conditions (1.8) can be regarded as an L^2-gradient flow on Γ of the surface energy

$$E_{\text{surf}}(\phi) = \int_\Gamma \left(\frac{\delta}{2}|\nabla_\Gamma\phi|^2 + \frac{\lambda}{2}|\phi|^2 + \frac{1}{\delta}G(\phi)\right) d\sigma, \tag{1.9}$$

where ∇_Γ represents the tangential or surface gradient operator defined on Γ. The Cahn–Hilliard equation (1.1) with the dynamic boundary conditions (1.8) is a gradient flow with the total free energy:

$$E(\phi) = E_{\text{bulk}}(\phi) + E_{\text{surf}}(\phi). \tag{1.10}$$

More precisely, it satisfies the following energy dissipation law:

$$\frac{d}{dt}E(\phi) = -\int_\Omega \mathbb{M}(\phi)|\nabla\mu|^2 d\boldsymbol{x} - \int_\Gamma |\mu_\Gamma|^2 d\sigma. \tag{1.11}$$

On the other hand, the authors in [11] (see also [9]) proposed to use

$$\phi_t = \Delta_\Gamma\mu_\Gamma, \qquad t > 0, \ \boldsymbol{x} \in \Gamma, \tag{1.12a}$$

$$\mu_\Gamma = -\delta\Delta_\Gamma\phi + \lambda\phi + \frac{1}{\delta}G'(\phi) + \epsilon\partial_{\boldsymbol{n}}\phi, \qquad t > 0, \ \boldsymbol{x} \in \Gamma, \tag{1.12b}$$

which can be regarded as an H^{-1}-gradient flow on Γ of the surface energy (1.9), and the Cahn–Hilliard equation (1.1) with the dynamic boundary conditions (1.12) is again a gradient flow with the total free energy (1.10) satisfying the following energy dissipation law:

$$\frac{d}{dt}E(\phi) = -\int_\Omega \mathbb{M}(\phi)|\nabla\mu|^2 d\boldsymbol{x} - \int_\Gamma |\nabla_\Gamma\mu_\Gamma|^2 d\sigma. \tag{1.13}$$

For the mathematical theory of the Cahn–Hilliard equation, coupled with the dynamic boundary conditions, as expressed in equation (1.8), the existence and uniqueness of solutions are first proved, then the convergence and the existence of exponential attractors are also studied under the assumptions on the nonlinearities in [12–16]. Numerous efforts have been made to develop efficient numerical schemes for the Cahn–Hilliard equation with dynamic boundary conditions. These include, but are not limited to, the finite difference scheme [17,18,10], the finite element method [19,8], and the finite-volume scheme [20]. The well-posedness of the Cahn–Hilliard equation with the dynamic boundary conditions as defined in equation (1.12) has been previously established in [11]. On the numerical side, a fully implicit, coupled second-order scheme was developed in [21]. In a separate study, Metzger et al. [22] constructed a fully discrete scheme, which is based on finite elements in space and first-order convex-splitting in time, demonstrated both energy stability and convergence. It should be noted that all schemes mentioned above require solving a nonlinear coupled system at each time step. In a more recent study, the authors of [23] considered a uniform Lipschitz potential. By

introducing a stabilizing term as in [24], they constructed a linear, first-order, and energy-stable scheme and derived a corresponding error analysis. However, this approach cannot be readily extended to second-order schemes or to non-uniformly Lipschitz nonlinear potentials. In all previous studies, the issue on how to efficiently solve the coupled system (with unknowns both in the bulk and at the boundary) at each time step, whether nonlinear or linear, is not quite resolved.

The main purpose of this paper is to develop a unified framework for constructing efficient and energy-stable numerical schemes for the Cahn–Hilliard system, addressing either equation (1.8) or (1.12). More precisely, our schemes employ MSAV approach [25,26] by introducing two SAVs: one for the unknowns in the bulk and the other for the unknowns at the boundary. Through this approach, we successfully develop a linear, second-order, and energy-stable scheme. The inherent coupling between the unknowns in the bulk and at the boundary in this linear system makes it challenging to find an efficient solution. To tackle this, we initially consider a generic spatial discretization, and then use the Shermann–Morrison–Woodbury formula to decouple the boundary unknowns from the bulk unknowns, essentially reducing the coupled system to a sequence of systems for the bulk unknowns that can be solved by the usual methods. In particular, we consider two specific situations: (i) If the domain is rectangular with one-periodic direction and one non-periodic direction, we use a Fourier approximation for the periodic direction and Legendre approximation for the non-periodic direction. Then, we can reduce the two dimensional coupled problem into a sequence of one-dimensional problems in the non-periodic direction that can be efficiently solved by using the Legendre-Galerkin method [27]; (ii) If the domain is rectangular with two non-periodic directions, we use the Legendre approximation for both directions, then the coupled problems for the bulk unknowns can be efficiently solved by the diagonalization method for coupled systems developed in [28]. To the best of our knowledge, the second-order schemes developed in this paper are the first linear, energy-stable, and essentially decoupled schemes for the Cahn–Hilliard system with both Allen–Cahn and Cahn–Hilliard types dynamic boundary conditions.

The rest of this paper is organized as follows. In the next section, a unified framework is introduced for the Cahn–Hilliard equation with both the Allen–Cahn and Cahn–Hilliard types of boundary conditions. In Section 3, we develop an unconditionally energy-stable scheme by using the MSAV approach. In Section 4, we propose an efficient algorithm to solve the linear but coupled system at each time step. Several numerical results are provided in Section 5 to validate our scheme, and to investigate the effect of different type dynamic boundary conditions on the phase evolution dynamics. Some concluding remarks are presented in Section 6.

2. A unified formulation

A unified form of the Cahn–Hillard system with dynamical boundary conditions can be written as

$$\partial_t \phi = \nabla \cdot (\mathbb{M}(\phi)\nabla \mu), \qquad \text{in } \Omega \times (0,T), \tag{2.1a}$$

$$\mu = -\epsilon \Delta \phi + \mathcal{N}'(\phi), \qquad \text{in } \Omega \times (0,T), \tag{2.1b}$$

$$\phi|_\Gamma = \psi; \quad \partial_{\boldsymbol{n}} \mu|_\Gamma = 0, \qquad \text{on } \Gamma \times (0,T), \tag{2.1c}$$

$$\partial_t \psi = -\mathcal{G}\mu_\Gamma, \qquad \text{on } \Gamma \times (0,T), \tag{2.1d}$$

$$\mu_\Gamma = -\delta \Delta_\Gamma \psi + \lambda \psi + \mathcal{N}_\Gamma'(\psi) + \epsilon \partial_{\boldsymbol{n}} \phi, \qquad \text{on } \Gamma \times (0,T), \tag{2.1e}$$

where $\mathcal{N}(\phi) = \frac{1}{\epsilon} F(\phi)$, $\mathcal{N}_\Gamma(\psi) = \frac{1}{\delta} G(\psi)$, $\mathbb{M}(\phi)$ is the mobility function, and $\mathcal{G}$ is a positive definite operator, e.g., $\mathcal{G} = I$ corresponds to (1.8) and $\mathcal{G} = -\Delta_\Gamma$ corresponds to (1.12). In the above, the independent unknown functions are ϕ, μ, and μ_Γ while $\psi = \phi|_\Gamma$.

Taking the inner products of (2.1a) with μ, (2.1b) with $-\partial_t \phi$, (2.1d) with μ_Γ, and (2.1e) with $-\partial_t \psi$, integrating by parts and summing up the results, we obtain the following energy dissipation law

$$\frac{d}{dt} E(\phi) = -\int_\Omega \mathbb{M}(\phi) |\nabla \mu|^2 d\boldsymbol{x} - \int_\Gamma \mathcal{G}\mu_\Gamma \cdot \mu_\Gamma d\sigma, \tag{2.2}$$

where $E(\phi)$ is the total free energy (1.10).

3. Numerical schemes

3.1. The MSAV approach

The scalar auxiliary variable (SAV) approach [25] is an effective strategy to construct efficient energy stable schemes by introducing one SAV, which is usually set as the square root of the nonlinear part of the free energy. However, if the nonlinear part of the free energy contains multiple disparate terms, such as the case here with the nonlinear bulk and surface energies, the one SAV approach may have severe time step constraints for accuracy [26]. In these cases, it is proposed in [26] to introduce multiple SAVs to treat these disparate nonlinear terms separately, leading to the so called MSAV approach. For our system (2.1), we introduce two SAVs for the bulk and surface free energies separately:

$$r(t) = \sqrt{E_1(\phi)} \quad \text{and} \quad q(t) = \sqrt{E_\Gamma(\psi)}, \tag{3.1}$$

where

$$E_1(\phi)=\int_\Omega \mathcal{N}(\phi)d\boldsymbol{x}+C_1 \quad \text{and} \quad E_\Gamma(\psi)=\int_\Gamma \mathcal{N}_\Gamma(\psi)d\sigma+C_\Gamma, \tag{3.2}$$

and the constants C_1 and C_Γ are chosen such that $E_1(\phi), E_\Gamma(\psi)>0$. Then, we expand the system (2.1) as:

$$\partial_t\phi=\nabla\cdot(\mathbb{M}(\phi)\nabla\mu), \tag{3.3a}$$

$$\mu=-\epsilon\Delta\phi+\frac{r}{\sqrt{E_1(\phi)}}\mathcal{N}'(\phi), \tag{3.3b}$$

$$\phi|_\Gamma=\psi; \quad \partial_{\boldsymbol{n}}\mu|_\Gamma=0, \tag{3.3c}$$

$$r_t=\frac{1}{2\sqrt{E_1(\phi)}}\int_\Omega \mathcal{N}'(\phi)\partial_t\phi\, d\boldsymbol{x}, \tag{3.3d}$$

$$\partial_t\psi=-\mathcal{G}\mu_\Gamma, \tag{3.3e}$$

$$\mu_\Gamma=-\delta\Delta_\Gamma\psi+\lambda\psi+\frac{q}{\sqrt{E_\Gamma(\psi)}}\mathcal{N}_\Gamma'(\psi)+\epsilon\partial_{\boldsymbol{n}}\phi, \tag{3.3f}$$

$$q_t=\frac{1}{2\sqrt{E_\Gamma(\psi)}}\int_\Gamma \mathcal{N}_\Gamma'(\psi)\partial_t\psi d\sigma. \tag{3.3g}$$

It is clear that with $r(0)=\sqrt{E_1(\phi)}|_{t=0}$ and $q(0)=\sqrt{E_\Gamma(\psi)}|_{t=0}$, the solution of (2.1) is also a solution of the above system.

3.2. Time discretization

Rather than directly discretizing the original system (2.1), we propose to work with the extended system (3.3), which provides enhanced flexibility and facilitates the development of efficient, linear, and unconditionally energy-stable numerical schemes. A second-order version of this system is formulated as follows

$$\frac{3\phi^{n+1}-4\phi^n+\phi^{n-1}}{2\delta t}=\nabla\cdot(\mathbb{M}(\bar{\phi}^{n+1})\nabla\mu^{n+1}), \tag{3.4a}$$

$$\mu^{n+1}=-\epsilon\Delta\phi^{n+1}+\frac{r^{n+1}}{\sqrt{E_1(\bar{\phi}^{n+1})}}\mathcal{N}'(\bar{\phi}^{n+1}), \tag{3.4b}$$

$$\phi^{n+1}|_\Gamma=\psi^{n+1}; \quad \partial_{\boldsymbol{n}}\mu^{n+1}|_\Gamma=0, \tag{3.4c}$$

$$\frac{3r^{n+1}-4r^n+r^{n-1}}{2\delta t}=\frac{1}{2\sqrt{E_1(\bar{\phi}^{n+1})}}\int_\Omega \mathcal{N}'(\bar{\phi}^{n+1})\frac{3\phi^{n+1}-4\phi^n+\phi^{n-1}}{2\delta t}d\boldsymbol{x}, \tag{3.4d}$$

$$\frac{3\psi^{n+1}-4\psi^n+\psi^{n-1}}{2\delta t}=-\mathcal{G}\mu_\Gamma^{n+1}, \tag{3.4e}$$

$$\mu_\Gamma^{n+1}=-\delta\Delta_\Gamma\psi^{n+1}+\lambda\psi^{n+1}+\frac{q^{n+1}}{\sqrt{E_\Gamma(\bar{\psi}^{n+1})}}\mathcal{N}_\Gamma'(\bar{\psi}^{n+1})+\epsilon\partial_{\boldsymbol{n}}\phi^{n+1}, \tag{3.4f}$$

$$\frac{3q^{n+1}-4q^n+q^{n-1}}{2\delta t}=\frac{1}{2\sqrt{E_\Gamma(\bar{\psi}^{n+1})}}\int_\Gamma \mathcal{N}_\Gamma'(\bar{\psi}^{n+1})\frac{3\psi^{n+1}-4\psi^n+\psi^{n-1}}{2\delta t}d\sigma. \tag{3.4g}$$

In the above and hereafter, for any function f, we denote $\bar{f}^{n+1}=2f^n-f^{n-1}$ which is an explicit $O(\delta t^2)$ approximation for $f(t^{n+1})$.

Theorem 1. *The scheme (3.4) conserves the mass in the bulk, i.e.,*

$$\int_\Omega \phi^{n+1}(\boldsymbol{x})d\boldsymbol{x}=\int_\Omega \phi^0(\boldsymbol{x})d\boldsymbol{x}.$$

If $\mathcal{G}=-\Delta_\Gamma$, it also conserves the mass on the surface, i.e.,

$$\int_\Gamma \psi^{n+1}(\boldsymbol{x})d\sigma=\int_\Gamma \psi^0(\boldsymbol{x})d\sigma.$$

Furthermore, it is unconditionally energy stable in the sense that

$$\tilde{E}_{total}(t^{n+1})-\tilde{E}_{total}(t^n)\le-\delta t\left[(\mathbb{M}(\bar{\phi}^{n+1})\nabla\mu^{n+1},\nabla\mu^{n+1})_\Omega+(\mathcal{G}\mu_\Gamma^{n+1},\mu_\Gamma^{n+1})_\Gamma\right], \tag{3.5}$$

where the modified energy is defined as

$$\tilde{E}_{total}(t^{n+1}) = \frac{\epsilon}{4}\left(\|\nabla\phi^{n+1}\|^2 + \|\nabla(2\phi^{n+1}-\phi^n)\|^2\right) + \frac{1}{2}\left((r^{n+1})^2 + (2r^{n+1}-r^n)^2\right)$$
$$+ \frac{\delta}{4}\left(\|\nabla_\Gamma\psi^{n+1}\|^2 + \|\nabla_\Gamma(2\psi^{n+1}-\psi^n)\|^2\right) + \frac{\lambda}{4}\left(\|\psi^{n+1}\|^2 + \|(2\psi^{n+1}-\psi^n)\|^2\right)$$
$$+ \frac{1}{2}\left((q^{n+1})^2 + (2q^{n+1}-q^n)^2\right).$$

Proof. The mass conservation in the bulk can be proved by integrating (3.4a) over Ω, while the mass conservation on the surface when $\mathcal{G} = -\Delta_\Gamma$ can be proved by integrating (3.4e) over Γ.

By taking the inner products of (3.4a) with μ^{n+1} and (3.4b) with $\frac{3\phi^{n+1}-4\phi^n+\phi^{n-1}}{2\delta t}$, and combining them with (3.4e)-(3.4f), we obtain

$$(\frac{3\phi^{n+1}-4\phi^n+\phi^{n-1}}{2\delta t}, \mu^{n+1})_\Omega + (\mathbb{M}(\bar{\phi}^{n+1})\nabla\mu^{n+1}, \nabla\mu^{n+1})_\Omega = 0, \tag{3.6a}$$

$$\begin{aligned}(\mu^{n+1}, \frac{3\phi^{n+1}-4\phi^n+\phi^{n-1}}{2\delta t})_\Omega &= \epsilon(\nabla\phi^{n+1}, \nabla\frac{3\phi^{n+1}-4\phi^n+\phi^{n-1}}{2\delta t})_\Omega \\ &+ (\frac{r^{n+1}}{\sqrt{E_1(\bar{\phi}^{n+1})}}\mathcal{N}'(\bar{\phi}^{n+1}), \frac{3\phi^{n+1}-4\phi^n+\phi^{n-1}}{2\delta t})_\Omega \\ &+ \delta(\nabla_\Gamma\psi^{n+1}, \nabla_\Gamma\frac{3\phi^{n+1}-4\phi^n+\phi^{n-1}}{2\delta t})_\Gamma \\ &+ \lambda(\phi^{n+1}, \frac{3\phi^{n+1}-4\phi^n+\phi^{n-1}}{2\delta t})_\Gamma \\ &+ (\frac{q^{n+1}}{\sqrt{E_\Gamma(\bar{\psi}^{n+1})}}\mathcal{N}_\Gamma'(\bar{\psi}^{n+1}), \frac{3\phi^{n+1}-4\phi^n+\phi^{n-1}}{2\delta t})_\Gamma \\ &+ (\mathcal{G}\mu_\Gamma^{n+1}, \mu_\Gamma^{n+1})_\Gamma.\end{aligned} \tag{3.6b}$$

Multiplying (3.4d) with $2r^{n+1}$, and (3.4g) with $2q^{n+1}$ lead to:

$$2r^{n+1}\frac{3r^{n+1}-4r^n+r^{n-1}}{2\delta t} = \frac{r^{n+1}}{\sqrt{E_1(\bar{\phi}^{n+1})}}\int_\Omega \mathcal{N}'(\bar{\phi}^{n+1})\frac{3\phi^{n+1}-4\phi^n+\phi^{n-1}}{2\delta t}d\boldsymbol{x}, \tag{3.7a}$$

$$2q^{n+1}\frac{3q^{n+1}-4q^n+q^{n-1}}{2\delta t} = \frac{q^{n+1}}{\sqrt{E_\Gamma(\bar{\psi}^{n+1})}}\int_\Gamma \mathcal{N}_\Gamma'(\bar{\psi}^{n+1})\frac{3\psi^{n+1}-4\psi^n+\psi^{n-1}}{2\delta t}d\sigma. \tag{3.7b}$$

By employing the technique of integration by parts, followed by summation of the resulting terms, and utilizing the identity

$$2a(3a-4b+c) = a^2 + (2a-b)^2 - b^2 - (2b-c)^2 + (a-2b+c)^2, \tag{3.8}$$

we obtain the desired result given in equation (3.5). □

4. Efficient implementation

Since the scheme (3.4) is a coupled linear system for $(\phi^{n+1}, \mu^{n+1}, \mu_\Gamma^{n+1}, r^{n+1}, q^{n+1})$, one can of course use a standard iterative or direct solver to solve the coupled linear system, but this is often inefficient, particularly when dealing with regular structures, such as a separable domain with a rectangular mesh, that one can explore.

We shall first decouple the computation of the two SAVs (r^{n+1}, q^{n+1}) from other unknowns. To this end, we write

$$\begin{aligned}&(\phi^{n+1}, \mu^{n+1}, \mu_\Gamma^{n+1}) = \\ &\quad(\phi_1^{n+1}, \mu_1^{n+1}, \mu_{\Gamma,1}^{n+1}) + r^{n+1}(\phi_2^{n+1}, \mu_2^{n+1}, \mu_{\Gamma,2}^{n+1}) + q^{n+1}(\phi_3^{n+1}, \mu_3^{n+1}, \mu_{\Gamma,3}^{n+1}).\end{aligned} \tag{4.1}$$

Substituting equation (4.1) to the above equations (3.4a)-(3.4b) and (3.4e)-(3.4f), and grouping the terms without (r^{n+1}, q^{n+1}), with r^{n+1} only, and with q^{n+1} only, we find that $(\phi_i^{n+1}, \mu_i^{n+1}, \mu_{\Gamma,i}^{n+1})$, $i = 1, 2, 3$ can be determined from the following decoupled systems:

$$\frac{3\phi_1^{n+1}-4\phi^n+\phi^{n-1}}{2\delta t} = \nabla\cdot(\mathbb{M}(\bar{\phi}^{n+1})\nabla\mu_1^{n+1}), \tag{4.2a}$$

$$\mu_1^{n+1} = -\epsilon\Delta\phi_1^{n+1}, \tag{4.2b}$$

$$\phi_1^{n+1}|_\Gamma = \psi_1^{n+1}; \quad \partial_{\boldsymbol{n}}\mu_1^{n+1}|_\Gamma = 0, \tag{4.2c}$$

$$\frac{3\psi_1^{n+1}-4\psi^n+\psi^{n-1}}{2\delta t} = -\mathcal{G}\mu_{\Gamma,1}^{n+1}, \tag{4.2d}$$

$$\mu_{\Gamma,1}^{n+1} = -\delta\Delta_\Gamma\psi_1^{n+1} + \lambda\psi_1^{n+1} + \epsilon\partial_{\boldsymbol{n}}\phi_1^{n+1}; \tag{4.2e}$$

$$\frac{3\phi_2^{n+1}}{2\delta t} = \nabla\cdot(\mathbb{M}(\bar{\phi}^{n+1})\nabla\mu_2^{n+1}), \tag{4.3a}$$

$$\mu_2^{n+1} = -\epsilon\Delta\phi_2^{n+1} + \frac{1}{\sqrt{E_1(\bar{\phi}^{n+1})}}\mathcal{N}'(\bar{\phi}^{n+1}), \tag{4.3b}$$

$$\phi_2^{n+1}|_\Gamma = \psi_2^{n+1}; \quad \partial_{\boldsymbol{n}}\mu_2^{n+1}|_\Gamma = 0, \tag{4.3c}$$

$$\frac{3\psi_2^{n+1}}{2\delta t} = -\mathcal{G}\mu_{\Gamma,2}^{n+1}, \tag{4.3d}$$

$$\mu_{\Gamma,2}^{n+1} = -\delta\Delta_\Gamma\psi_2^{n+1} + \lambda\psi_2^{n+1} + \epsilon\partial_{\boldsymbol{n}}\phi_2^{n+1}; \tag{4.3e}$$

and

$$\frac{3\phi_3^{n+1}}{2\delta t} = \nabla\cdot(\mathbb{M}(\bar{\phi}^{n+1})\nabla\mu_3^{n+1}), \tag{4.4a}$$

$$\mu_3^{n+1} = -\epsilon\Delta\phi_3^{n+1}, \tag{4.4b}$$

$$\phi_3^{n+1}|_\Gamma = \psi_3^{n+1}; \quad \partial_{\boldsymbol{n}}\mu_3^{n+1}|_\Gamma = 0, \tag{4.4c}$$

$$\frac{3\psi_3^{n+1}}{2\delta t} = -\mathcal{G}\mu_{\Gamma,3}^{n+1}, \tag{4.4d}$$

$$\mu_{\Gamma,3}^{n+1} = -\delta\Delta_\Gamma\psi_3^{n+1} + \lambda\psi_3^{n+1} + \frac{1}{\sqrt{E_\Gamma(\bar{\psi}^{n+1})}}\mathcal{N}_\Gamma'(\bar{\psi}^{n+1}) + \epsilon\partial_{\boldsymbol{n}}\phi_3^{n+1}. \tag{4.4e}$$

Notice that each of the three systems mentioned above can be written in the following generic coupled linear system

$$\alpha\phi = \nabla\cdot(\mathbb{M}(\boldsymbol{x})\nabla\mu + f(\boldsymbol{x}), \quad \partial_{\boldsymbol{n}}\mu|_\Gamma = 0, \tag{4.5a}$$

$$\mu = -\epsilon\Delta\phi + g(\boldsymbol{x}), \tag{4.5b}$$

$$\alpha\psi = -\mathcal{G}\mu + f_\Gamma(\boldsymbol{x}), \quad \phi|_\Gamma = \psi, \tag{4.5c}$$

$$\mu_\Gamma = -\delta\Delta_\Gamma\psi + \lambda\psi + g_\Gamma(\boldsymbol{x}) + \epsilon\partial_{\boldsymbol{n}}\phi. \tag{4.5d}$$

Hence, we shall only focus on developing an efficient solver for this generic coupled linear system.

4.1. A generic solution algorithm

Let $X_h \subset H^1(\Omega)$ and $X_h^\Gamma = X_h|_\Gamma$ be a pair of finite dimensional spaces. We consider a generic Galerkin spatial discretization for (4.5) as follows: find $\phi_h^{n+1}, \mu_h^{n+1} \in X_h$, $\mu_{\Gamma,h}^{n+1} \in X_h^\Gamma$ such that

$$\alpha(\phi_h, v_h)_\Omega = -(\mathbb{M}(\boldsymbol{x})\nabla\mu_h, \nabla v_h)_\Omega + (f(\boldsymbol{x}), v_h)_\Omega, \quad \forall v_h \in X_h, \tag{4.6a}$$

$$\begin{aligned}(\mu_h, v_h)_\Omega + (\mu_{\Gamma,h}, v_{\Gamma,h})_\Gamma = \epsilon(\nabla\phi_h, \nabla v_h)_\Omega + (g(\boldsymbol{x}), v_h)_\Omega + \delta(\nabla_\Gamma\psi_h, \nabla_\Gamma v_{\Gamma,h})_\Gamma \\ + \lambda(\psi_h, v_{\Gamma,h})_\Gamma + (g_\Gamma(\boldsymbol{x}), v_{\Gamma,h})_\Gamma, \quad \forall v_h \in X_h,\ v_{\Gamma,h} \in X_h^\Gamma,\end{aligned} \tag{4.6b}$$

$$\alpha(\psi_h, v_{\Gamma,h})_\Gamma = -(\mathcal{G}\mu_{\Gamma,h}, v_{\Gamma,h})_\Gamma + (f_\Gamma(\boldsymbol{x}), v_{\Gamma,h})_\Gamma, \quad \forall v_{\Gamma,h} \in X_h^\Gamma. \tag{4.6c}$$

Let $X_h = \mathrm{span}\{\xi_i\}_{i=1,\dots,N}$, then $X_h^\Gamma = X_h|_\Gamma = \mathrm{span}\{\xi_i|_\Gamma\}_{i=1,\dots,N} = \mathrm{span}\{\zeta_i\}_{i=1,\dots,k}$ where k is the number of nonzero basis function ξ_i on boundary. In this way, we can write the approximations as linear combinations of ξ_i and ζ_i that

$$\phi_h = \sum_{i=1}^N \boldsymbol{\phi}_i\xi_i, \quad \mu_h = \sum_{i=1}^N \boldsymbol{\mu}_i\xi_i, \quad \text{and} \quad \mu_{\Gamma,h} = \sum_{i=1}^k \boldsymbol{\mu}_{\Gamma i}\zeta_i.$$

Denote the mass matrices and the stiff matrices with respect to X_h by

$$M_{ij} = (\xi_i, \xi_j)_\Omega, \quad S_{ij} = (\nabla\xi_i, \nabla\xi_j)_\Omega, \quad S_{\mathbb{M}ij} = (\mathbb{M}(\boldsymbol{x})\nabla\xi_i, \nabla\xi_j)_\Omega, \quad 1 \le i, j \le N;$$

and the mass matrices and the stiff matrices with respect to X_h^Γ by

$$M_{\Gamma ij} = (\zeta_i, \zeta_j)_\Gamma, \quad S_{\Gamma ij} = (\nabla_\Gamma\zeta_i, \nabla_\Gamma\zeta_j)_\Gamma, \quad S_{\mathcal{G}ij} = (\mathcal{G}\zeta_i, \zeta_j)_\Gamma, \quad 1 \le i, j \le k.$$

We also denote

$$\boldsymbol{f}_i = (f(\boldsymbol{x}), \xi_i)_\Omega, \quad \boldsymbol{g}_i = (g(\boldsymbol{x}), \xi_i)_\Omega, \ 1 \le i \le N;$$

and

$$\boldsymbol{f}_{\Gamma i} = (f_\Gamma(\boldsymbol{x}), \zeta_i)_\Gamma, \quad \boldsymbol{g}_{\Gamma i} = (g_\Gamma(\boldsymbol{x}), \zeta_i)_\Gamma, \ 1 \le i \le k.$$

For better representation, we also introduce following matrices and vectors that

$$\tilde{M}_\Gamma = \begin{bmatrix} M_\Gamma \\ 0_{(N-k)\times k} \end{bmatrix}, \quad \hat{M}_\Gamma = \begin{bmatrix} M_\Gamma & 0_{k\times(N-k)} \\ 0_{(N-k)\times k} & 0_{(N-k)\times(N-k)} \end{bmatrix}, \quad \hat{S}_\Gamma = \begin{bmatrix} S_\Gamma & 0_{k\times(N-k)} \\ 0_{(N-k)\times k} & 0_{(N-k)\times(N-k)} \end{bmatrix},$$

and

$$\hat{\boldsymbol{g}}_\Gamma = \begin{bmatrix} \boldsymbol{g}_\Gamma \\ \boldsymbol{0}_{N-k} \end{bmatrix}.$$

With these notations, the full discretization scheme (4.6) reduces to the following matrix form:

$$\begin{bmatrix} \alpha M & S_{\mathbb{M}} & 0 \\ -(\epsilon S + \delta \hat{S}_\Gamma + \lambda \hat{M}_\Gamma) & M & \tilde{M}_\Gamma \\ \alpha \tilde{M}_\Gamma^T & 0 & S_{\mathcal{G}} \end{bmatrix} \begin{bmatrix} \boldsymbol{\phi} \\ \boldsymbol{\mu} \\ \boldsymbol{\mu}_\Gamma \end{bmatrix} = \begin{bmatrix} \boldsymbol{f} \\ \boldsymbol{g} + \hat{\boldsymbol{g}}_\Gamma \\ \boldsymbol{f}_\Gamma \end{bmatrix}, \tag{4.7}$$

which can be rewritten as

$$\begin{bmatrix} B & \boldsymbol{b} \\ \boldsymbol{c}^T & S_{\mathcal{G}} \end{bmatrix} \begin{bmatrix} \boldsymbol{\varphi} \\ \boldsymbol{\mu}_\Gamma \end{bmatrix} = \begin{bmatrix} \boldsymbol{h} \\ \boldsymbol{f}_\Gamma \end{bmatrix}, \tag{4.8}$$

where $\boldsymbol{\varphi} = (\boldsymbol{\phi}, \boldsymbol{\mu})^T$ and

$$B = \begin{bmatrix} \alpha M & S_{\mathbb{M}} \\ -(\epsilon S + \delta \hat{S}_\Gamma + \lambda \hat{M}_\Gamma) & M \end{bmatrix}. \tag{4.9}$$

Note that, with proper basis selection, the dimension of X_h^Γ or the rank of $S_{\mathcal{G}}$, k, can be much less than N, the dimension of X_h, i.e., $k \ll N$. Since the rank of B is $2N \gg k$, we can obtain $\boldsymbol{\mu}_\Gamma$ by solving a $k \times k$ Schur-compliment system

$$(S_{\mathcal{G}} - \boldsymbol{c}^T B^{-1} \boldsymbol{b}) \boldsymbol{\mu}_\Gamma = \boldsymbol{l}_\Gamma - \boldsymbol{c}^T B^{-1} \boldsymbol{h}. \tag{4.10}$$

The main cost of solving the above system is to evaluate $B^{-1}\boldsymbol{b}$ and $B^{-1}\boldsymbol{h}$. We describe below how this can be done efficiently.

Note that the ranks of $\hat{S}_\Gamma$ and $\hat{M}_\Gamma$ are at most k, which indicates that we can write $\delta \hat{S}_\Gamma + \lambda \hat{M}_\Gamma = X_{2N\times k} Y_{k\times 2N}$ so that we can split B as

$$\begin{aligned} B &= \begin{bmatrix} \alpha M & S_{\mathbb{M}} \\ -(\epsilon S + \delta \hat{S}_\Gamma + \lambda \hat{M}_\Gamma) & M \end{bmatrix} = \begin{bmatrix} \alpha M & S_{\mathbb{M}} \\ -\epsilon S & M \end{bmatrix} + \begin{bmatrix} 0 & 0 \\ -XY & 0 \end{bmatrix} \\ &:= A - \begin{bmatrix} 0 \\ X \end{bmatrix} \begin{bmatrix} Y & 0 \end{bmatrix} = A - UV. \end{aligned} \tag{4.11}$$

Then, applying this Sherman–Morrison–Woodbury formula [29], we find

$$\begin{bmatrix} \alpha M & S_{\mathbb{M}} \\ -(\epsilon S + \delta \hat{S}_\Gamma + \lambda \hat{M}_\Gamma) & M \end{bmatrix}^{-1} = (A - UV)^{-1} = A^{-1} + A^{-1} U (I_k - V A^{-1} U)^{-1} V A^{-1}. \tag{4.12}$$

Hence, evaluating $B^{-1}\boldsymbol{b}$ can be accomplished by evaluating $A^{-1}\boldsymbol{b}$ with about k different $\boldsymbol{b}$.

We observe that the matrix

$$A = \begin{bmatrix} \alpha M & S_{\mathbb{M}} \\ -\epsilon S & M \end{bmatrix}, \tag{4.13}$$

which is a perturbation of matrix B, is the system matrix related to the discretization of the system (4.5a)-(4.5b) with the additional boundary condition $\partial_n \phi|_\Gamma = 0$. In many situations, e.g., if the domain is separable and $\mathbb{M}(\boldsymbol{x})$ is a constant, fast evaluation of $A^{-1}\boldsymbol{b}$ is available by using the fast Fourier transforms (FFT) or the matrix diagonalization method [30,31], see some examples given below.

4.2. The case with one non-periodic direction

In many applications, the problem only has one non-periodic direction. In this case, we can first take (discrete) Fourier transform in the periodic direction(s). Then, in the case of constant mobility, the corresponding linear system (4.5) reduces to an one-dimensional problem for each of the Fourier modes, and Γ reduces to two points so $k = 2$. On the other hand, for each of the Fourier modes, A in (4.13) corresponds to an approximation of a coupled 1-D second-order system with homogeneous Neumann boundary conditions, that can be efficiently solved.

Consider for example a 3-D domain with two periodic boundary conditions, and we use a combined Fourier-Legendre spectral method with $N \times N \times M$ unknowns where N is the number of unknowns in the periodic direction, and M is the unknown in the non-periodic direction. Then, for each of the Fourier modes, the coupled 1-D second-order system with homogeneous Neumann boundary conditions can be solved by the Legendre-Galerkin method [27] in $O(M)$ operations, considering the cost of transform

Table 1
Parameter values for accuracy test.

Parameter	Value	Parameter	Value
ϵ, δ	0.5	λ	1
m	1	l_0, m_Γ	1
C_1	10	C_Γ	10
t_0	0	t_f	1

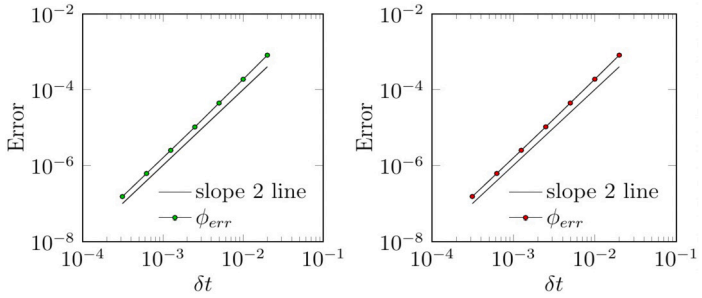

Fig. 1. Accuracy test for different type boundary conditions: Allen–Cahn type (left), Cahn–Hilliard type (right).

between the physical and frequency spaces using a Chebyshev-Legendre approach [32], the total cost of solving the linear system (4.7) will be $O(N^2 M \log N \log M)$ which is quasi-optimal in terms of number of unknowns.

4.3. The case with two non-periodic directions

For problems in a separable domain having two non-periodic directions, fast evaluation of $A^{-1}\boldsymbol{b}$ can be achieved by using the matrix diagonalization method [30,31]. Consider for instance a two-dimensional rectangular domain, then A in (4.13) corresponds to an approximation of a coupled 2-D second-order system with homogeneous Neumann boundary conditions which can be solved efficiently by using the matrix diagonalization method for coupled systems developed in [28] in $O(N^3)$ operations with N being the number of unknowns in each direction. This operation count can be further reduced to $O(N^2 \log N)$ if one uses the Chebyshev-Legendre approach [32].

Similarly, fast evaluation of $A^{-1}\boldsymbol{b}$ can also be achieved for cylindrical domains [33].

5. Numerical results

In this section, we conduct several numerical experiments in two dimensions to validate our schemes, and to investigate the effect of different dynamical boundary conditions with $\mathcal{G} = l_0 I$ (Allen–Cahn type) or $\mathcal{G} = m_\Gamma(-\Delta_\Gamma)$ (Cahn–Hilliard type). To fix the idea, we consider (2.1a)-(2.1e) with the classical double well energy functional

$$\mathcal{N}(\phi) = \frac{1}{4\epsilon}(\phi^2 - 1)^2, \quad \mathcal{N}_\Gamma(\phi) = \frac{1}{4\delta}(\psi^2 - 1)^2. \tag{5.1}$$

We perform two sets of numerical experiments in 2D, one with two non-periodic directions, and the other with only one periodic direction. In all numerical tests, the second-order SAV scheme (3.4) is used.

5.1. Rectangular domains with one periodic direction

We consider $\Omega = L_x \times L_y$ with periodic boundary conditions in the x-direction. Unless otherwise specified, the mobility is set to be a constant, i.e., $\mathbb{M}(\phi) = m$.

5.1.1. Accuracy test

We first perform numerical simulations to test the convergence rates of the scheme. The computational domain is set as $\Omega = [0, 2) \times [0, 2)$, and we use 50×50 Fourier-Legendre modes to discretize the space variables and take the mesh refinement test with the following function

$$\phi(x, y, t) = \cos(\pi x)\cos(\pi y)e^{-t}.$$

The parameters are defined as shown in Table 1.

In Fig. 1, we list the errors of the phase variable ϕ between the numerically simulated solution and the exact solution at $t_f = 1$, measured in the L^∞ norm. We observe that our scheme almost perfect matches the second-order accuracy in time.

Table 2
Simulation parameter values for coarsening process.

Parameter	Value	Parameter	Value
ϵ, δ	1	λ	0.5
m	1	l_0	1
C	1	C_Γ	1
$\mathcal{N}(\phi)$	$\frac{1}{8\epsilon}(\phi^2-1)^2$	$\mathcal{N}_\Gamma(\psi)$	$\frac{1}{2\epsilon}\psi^2$

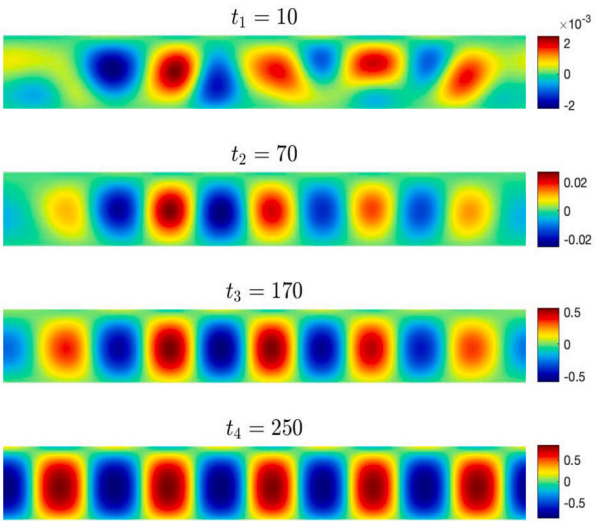

Fig. 2. Snapshots of solution for coarsening process with Allen–Cahn type dynamical boundary condition at time 10, 70, 170, 250.

5.1.2. Coarsening process

To further validate our numerical scheme, we simulate the spinodal decomposition of the systems with the Allen–Cahn type dynamic boundary conditions.

We set $\Omega = [0, 80) \times (0, 10)$, and use the initial condition

$$\phi(x, y, 0) = 0.01 \times (2\text{Rand}(x, y) - 1), \tag{5.2}$$

where Rand(x, y) is the uniformly distributed random function in Ω. We set the time step $\delta t = 0.1$ and use 128×30 Fourier-Legendre modes. We use the parameters listed in Table 2, which are similar to those employed in [10]. Snapshots of the phase variable ϕ are shown in Fig. 2. We observe that neither component is preferentially attracted by the wall, which is comparable to those in [10].

5.1.3. Droplet evolution

Rewrite $E_{\text{bulk}}(\phi)$ and $E_{\text{surf}}(\psi)$ as [25]

$$\begin{aligned} E_{\text{bulk}}(\phi) &= \int_\Omega \frac{\epsilon}{2}|\nabla\phi|^2 + \frac{s_1}{2\epsilon}\phi^2 + \frac{1}{4\epsilon}(\phi^2 - 1 - s_1)^2 - \frac{s_1^2 + 2s_1}{4\epsilon} d\boldsymbol{x}, \\ E_{\text{surf}}(\psi) &= \int_\Gamma \left(\frac{\delta}{2}|\nabla_\Gamma\psi|^2 + \frac{\lambda}{2}|\psi|^2 + \frac{s_2}{2\epsilon}\psi^2 + \frac{1}{4\delta}(\psi^2 - 1 - s_2)^2 - \frac{s_2^2 + 2s_2}{4\epsilon} \right) d\sigma, \end{aligned} \tag{5.3}$$

and drop the constant in the free energy and let $\mathcal{N}(\phi) = \frac{1}{4\epsilon}(\phi^2 - 1 - s_1)^2$ and $\mathcal{N}_\Gamma(\psi) = \frac{1}{4\epsilon}(\psi^2 - 1 - s_2)^2$, and modify (3.4b) and (3.4f) into

$$\begin{aligned} \mu^{n+1} &= -\epsilon\Delta\phi^{n+1} + \frac{s_1}{\epsilon}\phi^{n+1} + \frac{r^{n+1}}{\sqrt{E_1(\bar{\phi}^{n+1})}}\mathcal{N}'(\bar{\phi}^{n+1}), \\ \mu_\Gamma^{n+1} &= -\delta\Delta_\Gamma\psi^{n+1} + \lambda\psi^{n+1} + \frac{s_2}{\epsilon}\psi^{n+1} + \frac{q^{n+1}}{\sqrt{E_\Gamma(\bar{\psi}^{n+1})}}\mathcal{N}_\Gamma'(\bar{\psi}^{n+1}) + \epsilon\partial_{\boldsymbol{n}}\phi^{n+1}. \end{aligned} \tag{5.4}$$

We set $\Omega = (0, 2) \times (0, 1)$ with initially a square shaped droplet centered at $(1, 0.25)$ (see Fig. 3). We employ a grid resolution of 100×50 Fourier-Legendre modes with a time step of $\delta t = 5 \times 10^{-4}$ and set the simulation parameters as specified in Table 3. The phase value inside the droplet is set to be 1 and outside the droplet to be -1.

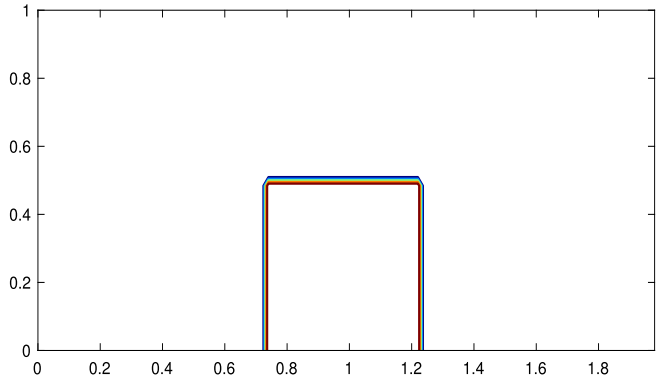

Fig. 3. The initial square shaped droplet.

Table 3
Simulation parameter values for droplet evolution.

Parameter	Value	Parameter	Value
ϵ, δ	0.02	λ	0
m	1	l_0, m_Γ	1
C, C_Γ	1	s_1, s_2	2
$\mathcal{N}(\phi)$	$\frac{1}{4\epsilon}(\phi^2-1)^2$	$\mathcal{N}_\Gamma(\psi)$	$\frac{1}{4\delta}(\psi^2-1)^2$

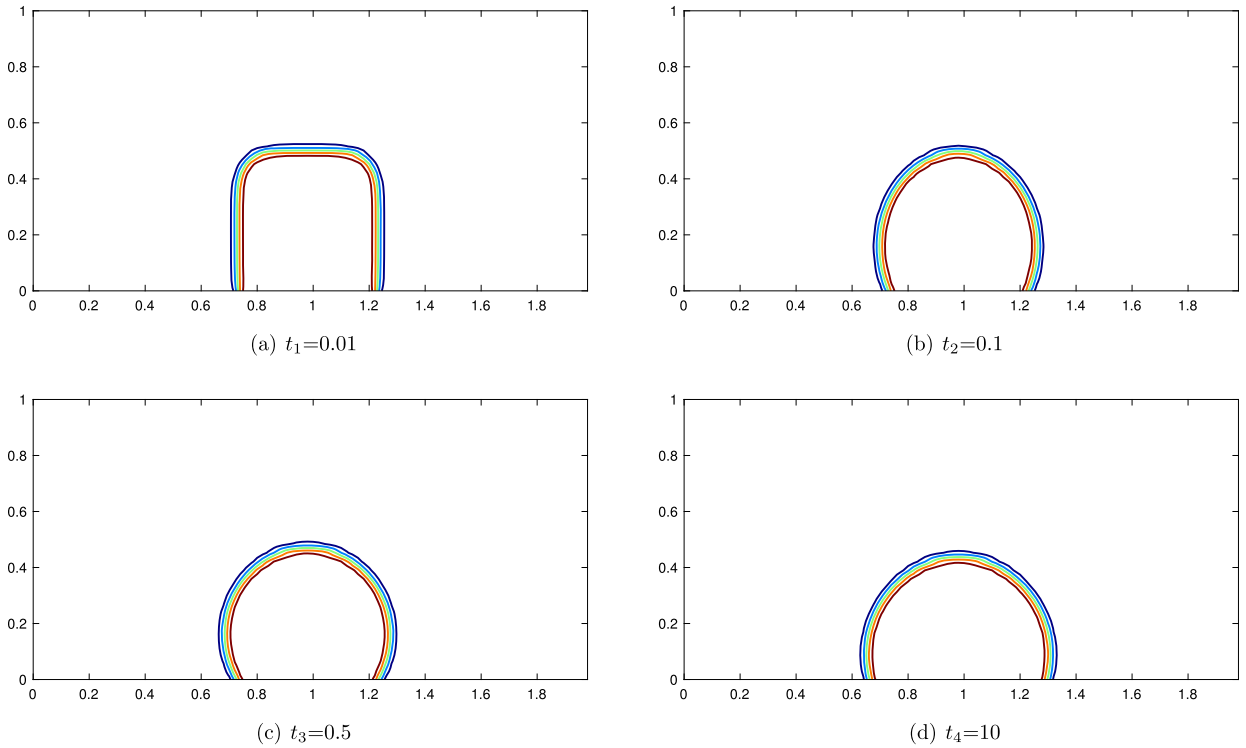

Fig. 4. Snapshots of solution for droplet evolution with Allen–Cahn type dynamical boundary conditions at time 0.01, 0.1, 0.5, 10.

We simulate the dynamics of the droplet from $t = 0$ to $t_f = 10$. The evolution of the droplet with the Allen–Cahn (resp. Cahn–Hilliard) type boundary conditions is presented in Fig. 4 (resp. Fig. 5). We observe that with the Allen–Cahn type boundary conditions, the contact area with the boundary increases as the droplets bulk decreases, while with Cahn-Hilliard type boundary conditions, the area of contact with the boundary is preserved during the evolution. These numerical results are all in good agreement with the results shown in [34,35].

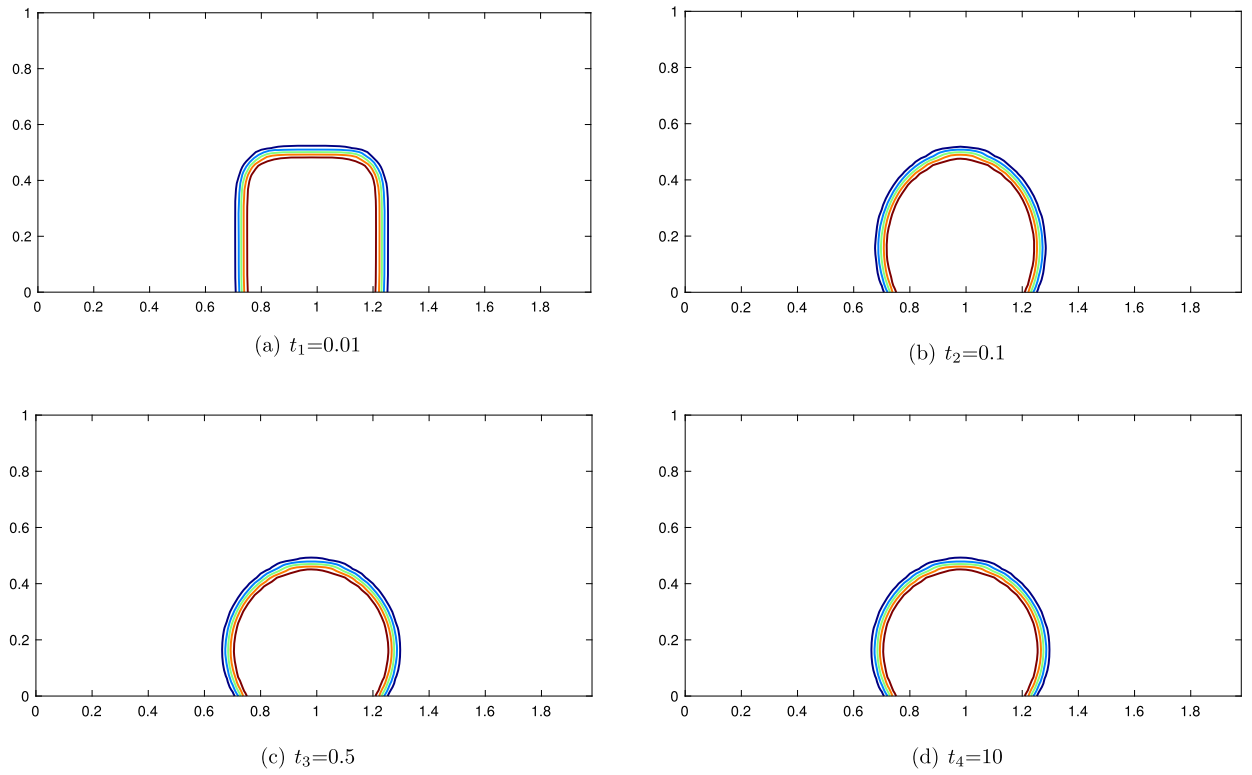

Fig. 5. Snapshots of solution for droplet evolution with Cahn–Hilliard type dynamical boundary conditions at time 0.01, 0.1, 0.5, 10.

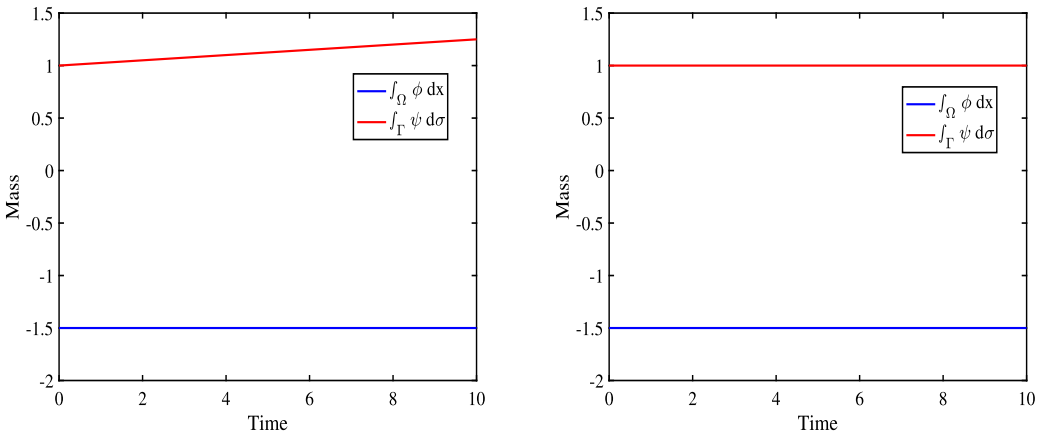

Fig. 6. Mass curves for bulk and surface of the droplet evolution: Allen–Cahn type (left), Cahn–Hilliard type (right).

The evolution of mass curves $\int_\Omega \phi d\boldsymbol{x}$ and $\int_\Gamma \psi d\sigma$ with Allen–Cahn and Cahn–Hilliard type dynamic boundary conditions is shown in Fig. 6. We observe that for both type of boundary conditions, $\int_\Omega \phi d\boldsymbol{x}$ is preserved, but $\int_\Gamma \psi d\sigma$ decreases with the Allen–Cahn type dynamical boundary conditions while it remains the same with the Cahn–Hilliard type dynamical boundary conditions.

5.1.4. Cases with different potential functions

In the numerical experiments mentioned above, the surface potential $\mathcal{N}_\Gamma(\psi)$ is chosen as the classical double-well potential, here we consider the typical moving contact line problems, namely,

$$\mathcal{N}_\Gamma(\psi) = \frac{\gamma}{2\delta} cos(\theta_s) sin(\frac{\pi}{2}\psi), \tag{5.5}$$

where θ_s stands for the static contact angle. We choose the same parameters as those in the previous subsection with $\gamma = \frac{2\sqrt{2}}{3}$ and $cos(\theta_s) = \pm\frac{1}{2}$. We employ 100×50 Fourier-Legendre modes with a time step of $\delta t = 1 \times 10^{-5}$ in this simulation. The square-shaped

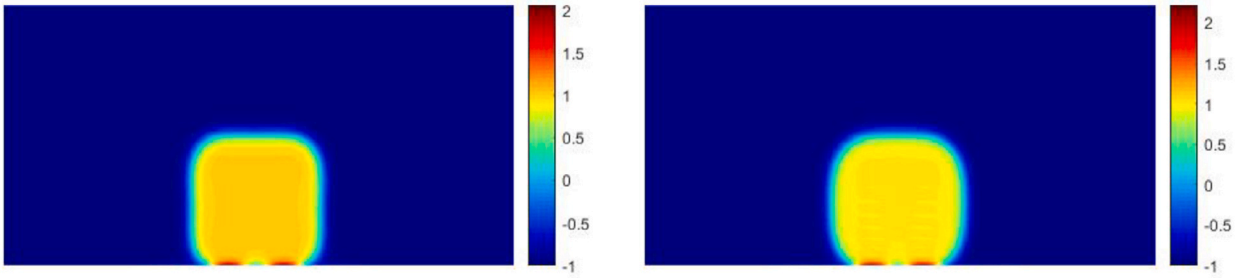

(a) t_1=0.0005 (b) t_2=0.001

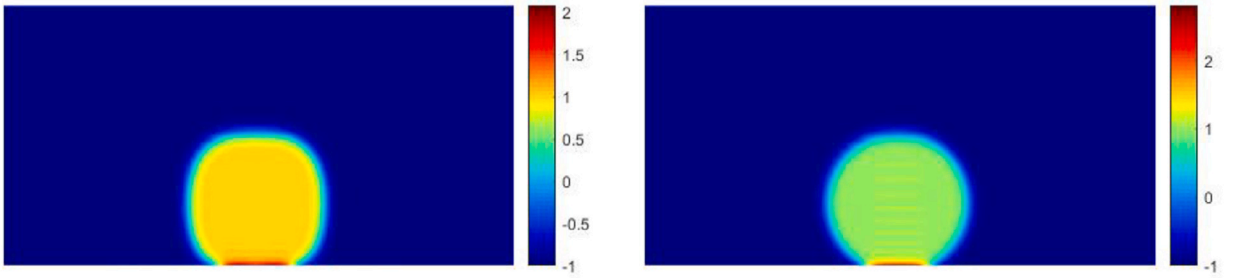

(c) t_3=0.0015 (d) t_4=0.02

Fig. 7. Snapshots of solution depicting droplet evolution under Cahn–Hilliard type dynamic boundary conditions characterized by the surface potential $\mathcal{N}_\Gamma(\psi)$ $(cos(\theta_s) = \frac{1}{2})$ at time 0.01, 0.1, 0.5, 10.

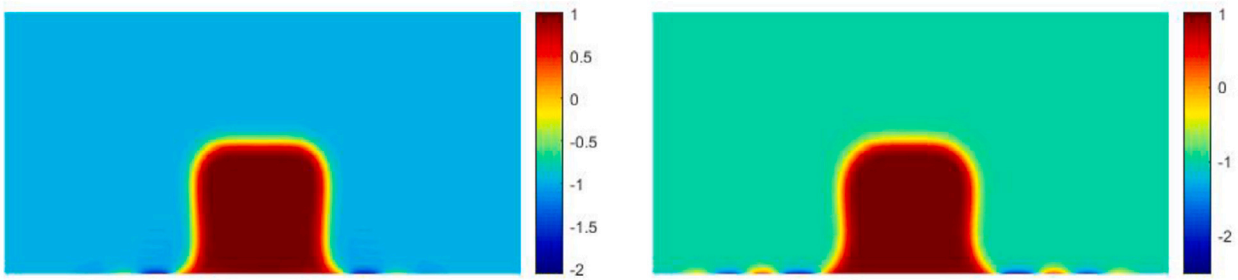

(a) t_1=0.0005 (b) t_2=0.001

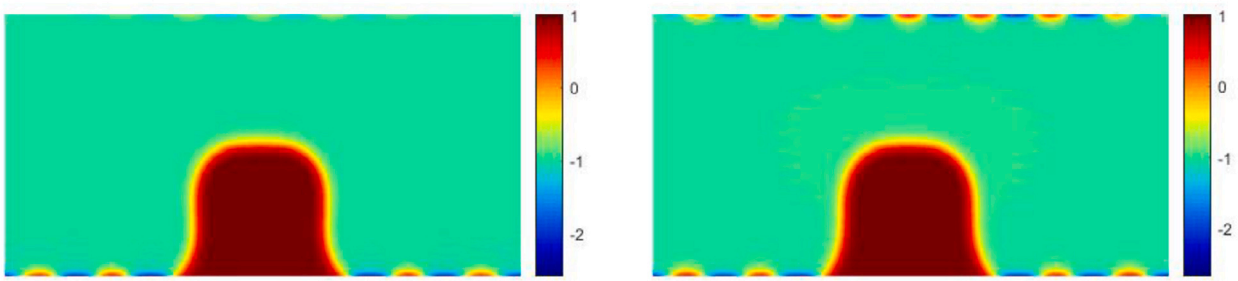

(c) t_3=0.0015 (d) t_4=0.02

Fig. 8. Snapshots of solution depicting droplet evolution under Cahn–Hilliard type dynamic boundary conditions characterized by the surface potential $\mathcal{N}_\Gamma(\psi)$ $(cos(\theta_s) = -\frac{1}{2})$.

droplet also tends to attain the circle with time in Figs. 7-8. The values of ϕ and ψ are not confined in $[-1, +1]$, since the conservation of mass both in the bulk and on the boundary as shown in Fig. 9. All of these numerical results are in good agreement with the results shown in [35,36].

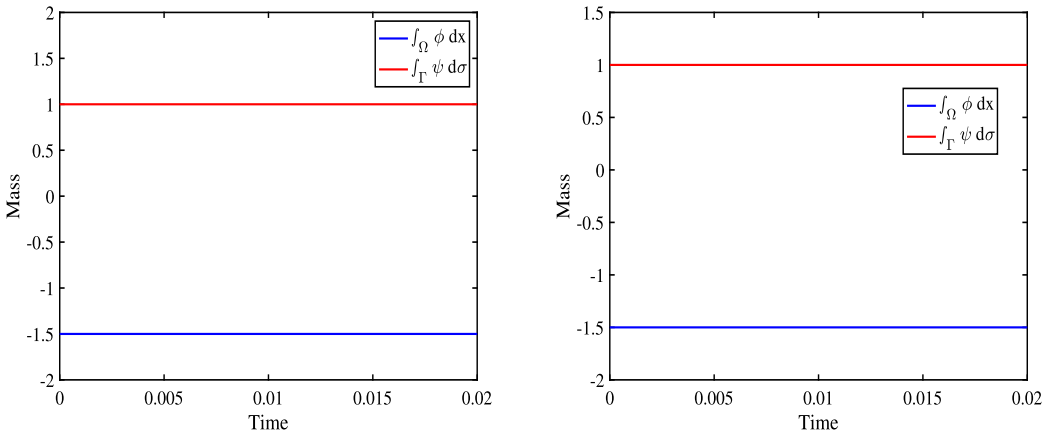

Fig. 9. Mass curves for bulk and surface of the droplet evolution: $cos(\theta_s) = \frac{1}{2}$ (left), $cos(\theta_s) = -\frac{1}{2}$ (right).

Table 4
Parameter values for accuracy test.

Parameter	Value	Parameter	Value
ϵ, δ	0.2	λ	1
m	0.01	l_0, m_Γ	0.01
C_1	10	C_Γ	10
t_0	0	t_f	1

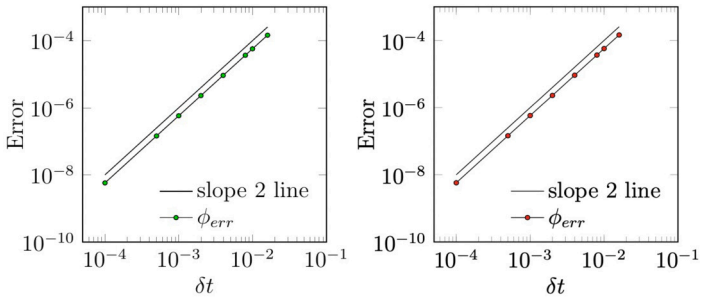

Fig. 10. Accuracy test for different type boundary conditions: Cahn–Hilliard type (left), Allen–Cahn type (right).

5.2. Rectangular domains with two non-periodic directions

5.2.1. Accuracy test

We first validate the scheme (3.4) with a manufactured analytical solution in $\Omega = [-1, 1]^2$ that

$$\phi(x, y, t) = \sin(\pi x)\sin(\pi y)e^t, \tag{5.6}$$

$$\mu(x, y, t) = \cos(\pi x)\cos(\pi y)e^t, \tag{5.7}$$

$$\mu_\Gamma(x, y, t) = \cos(\pi x)\cos(\pi y)e^t. \tag{5.8}$$

We set the mobility to be a constant, i.e., $\mathbb{M}(\phi) = m$. We choose $N = 20$ so that the spatial discretization error is negligible compared with the time discretization error and set the simulation parameters as Table 4. The L^∞ errors vs. time step are plotted in Fig. 10. We observe second-order convergence for both the Cahn–Hilliard and Allen–Cahn type dynamic boundary conditions.

5.2.2. Phase separation

We consider an initial configuration in domain $\Omega = [0, 1]^2$ that

$$\phi_0(x, y) = 0.1 \max\{\sin(\pi x), \sin(\pi y)\}. \tag{5.9}$$

We simulate the phase separation process with two different dynamic boundary conditions (1.8) and (1.12) with parameters in Table 5. The results are plotted in Figs. 12 and 13. We observe that with different type of dynamic boundary conditions, the dynamic

Table 5
Simulation parameter values for phase separation.

Parameter	Value	Parameter	Value
ϵ, δ	0.02	λ	0
m	0.02	l_0, m_Γ	0.02
C	0	C_Γ	0
δt	4×10^{-5}	t_f	4

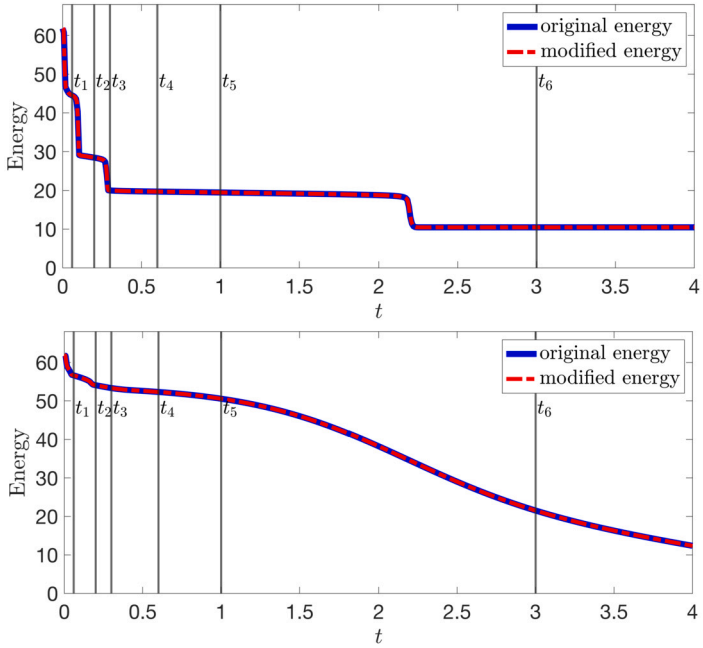

Fig. 11. Energy curves of phase separation: Cahn–Hilliard type (up), Allen–Cahn type (down).

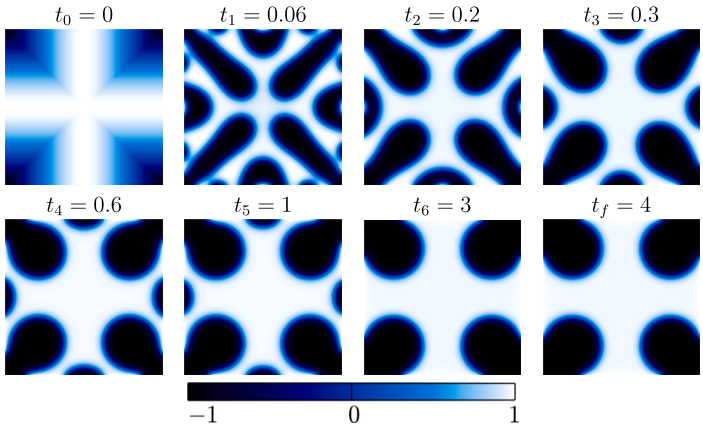

Fig. 12. Snapshots of solution for phase separation with Cahn–Hilliard type dynamical boundary conditions. The selected times are marked on energy curve in Fig. 11, and we normalized $\phi/max(\phi)$ at the time instants as indicated.

processes of the phase separation are different, particularly at the boundary. For the Cahn-Hilliard type of boundary conditions (1.12), the area of each phase at the boundary is conserved, while for the Allen-Cahn type boundary conditions (1.8), the area of each phase is not conserved, and the black phase at the boundary eventually reduces to almost zero (Fig. 14). These results are in good agreements with those in [22,37].

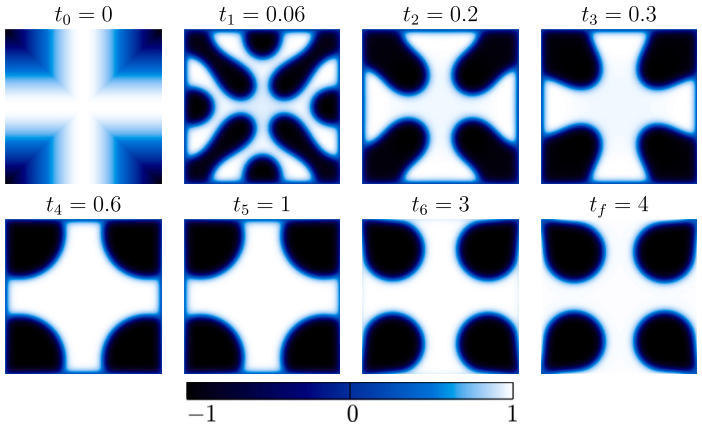

Fig. 13. Snapshots of solution for phase separation with Allen–Cahn type dynamical boundary conditions. The selected times are the same as in Fig. 12 for the sake of comparison, and we normalized $\phi/max(\phi)$ at the time instants as indicated.

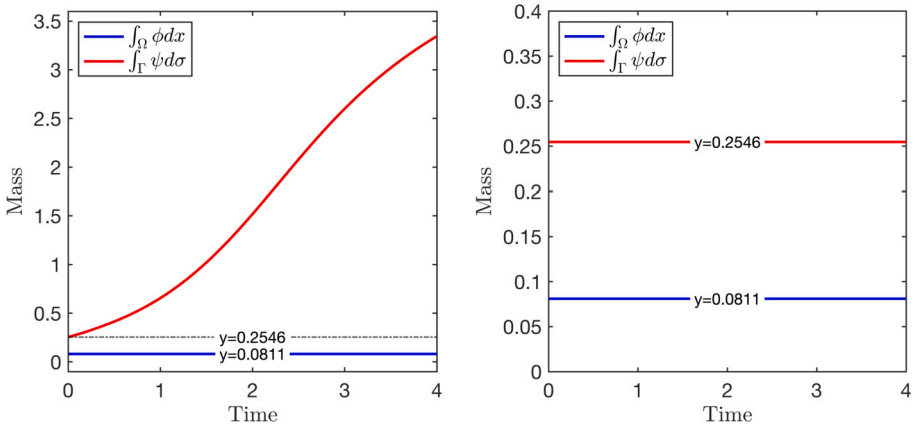

Fig. 14. Mass curves for bulk and surface of the phase separation: Allen–Cahn type (left), Cahn–Hilliard type (right).

Table 6
Simulation parameter values for spinodal decomposition.

Parameter	Value	Parameter	Value
ϵ, δ	0.02	λ	1
m	0.01	l_0, m_Γ	0.01
C	0	C_Γ	0
δt	1×10^{-4}	t_f	20

5.2.3. Spinodal decomposition

Next, we conduct a simulation of spinodal decomposition with the parameters in Table 6, and a random initial configuration in domain $\Omega = [0, 1]^2$ that

$$\phi_0(x, y) = 0.1\text{Rand}(x, y). \tag{5.10}$$

The numerical results are plotted in Figs. 16 and 17. We observe once again that during the spinodal decomposition process, the area of each phase at the boundary is conserved with Cahn-Hilliard type boundary conditions, while the blue phase evolves into a circle and is completely separated from the boundary.

6. Concluding remarks

In this paper, we introduced a unified framework to deal with the Cahn-Hilliard equation with two different types of dynamic boundary conditions, and developed a second-order, linear and energy stable scheme based on the MSAV approach. At each time step, the scheme leads to a linear system which couples the unknowns in the bulk and at the boundary. We designed efficient algorithms for

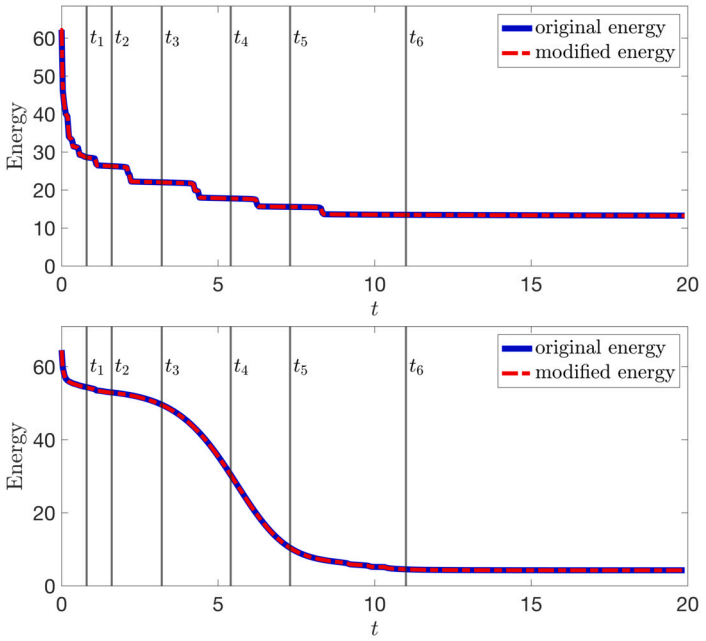

Fig. 15. Energy curves of the spinodal decomposition process: Cahn–Hilliard type (up), Allen–Cahn type (down).

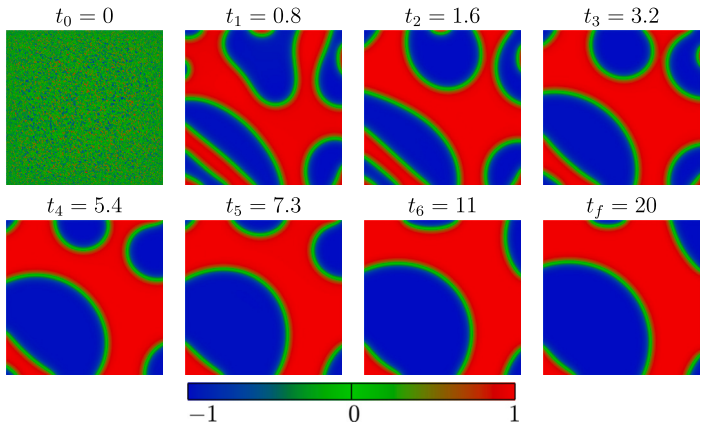

Fig. 16. Snapshots of solution for spinodal decomposition with Cahn–Hilliard type boundary conditions. The selected times are marked on the energy curve in Fig. 15, and we normalized $\phi/max(\phi)$ at the time instants as indicated. (For interpretation of the colors in the figure(s), the reader is referred to the web version of this article.)

solving this coupled linear system. In particular, in the case of separable domains with one or two non-periodic boundary conditions, we presented efficient spectral methods which can solve the coupled linear system with quasi-optimal computational complexity. Furthermore, we conducted several numerical experiments to validate the proposed scheme, and to investigate the effect of different dynamical boundary conditions on the dynamics of phase evolution under different scenarios.

CRediT authorship contribution statement

Xinyu Liu: Conceptualization, Formal analysis, Validation, Writing – original draft, Writing – review & editing. **Jie Shen:** Conceptualization, Formal analysis, Investigation, Project administration, Writing – review & editing. **Nan Zheng:** Formal analysis, Investigation, Methodology, Validation, Writing – original draft, Writing – review & editing.

Declaration of competing interest

The authors declare that they have no known competing financial interests or personal relationships that could have appeared to influence the work reported in this paper.

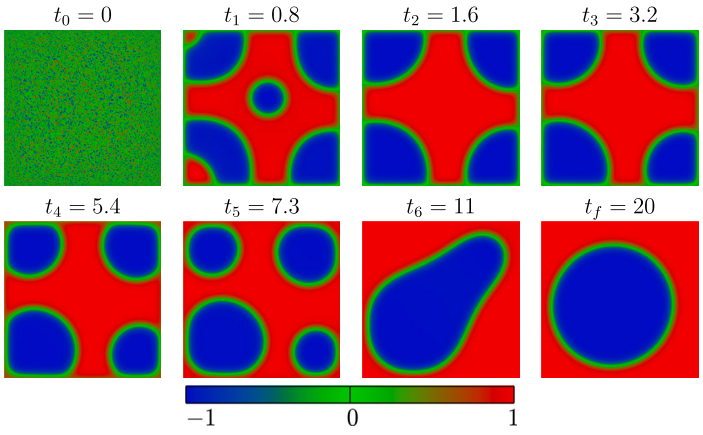

Fig. 17. Snapshots of solution for spinodal decomposition with Allen–Cahn type boundary conditions. The selected times are the same as in Fig. 16 for the sake of comparison, and we normalized $\phi/max(\phi)$ at the time instants as indicated.

Data availability

No data was used for the research described in the article.

Acknowledgements

This work is supported in part by NSFC grant 12371409, and by The Hong Kong Polytechnic University Postdoctoral Research Fund 1-W22P.

References

[1] J.W. Cahn, J.E. Hilliard, Free energy of a nonuniform system. I. Interfacial free energy, J. Chem. Phys. 28 (1958) 258–267.
[2] C.M. Elliott, S. Zheng, On the Cahn-Hilliard equation, Arch. Ration. Mech. Anal. 96 (1986) 339–357.
[3] S. Zheng, Asymptotic behavior of solution to the Cahn-Hillard equation, Appl. Anal. 23 (1986) 165–184.
[4] R.L. Pego, Front migration in the nonlinear Cahn-Hilliard equation, Proc. R. Soc. Lond. Ser. A, Math. Phys. Sci. 422 (1989) 261–278.
[5] P.W. Bates, P.C. Fife, The dynamics of nucleation for the Cahn-Hilliard equation, SIAM J. Appl. Math. 53 (1993) 990–1008.
[6] T. Qian, X.-P. Wang, P. Sheng, Molecular scale contact line hydrodynamics of immiscible flows, Phys. Rev. E 68 (2003) 016306.
[7] W. Ren, W. E, Derivation of continuum models for the moving contact line problem based on thermodynamic principles, Commun. Math. Sci. 9 (2011) 597–606.
[8] L. Cherfils, M. Petcu, M. Pierre, A numerical analysis of the Cahn-Hilliard equation with dynamic boundary conditions, Discrete Contin. Dyn. Syst. 27 (2010) 1511–1533.
[9] G.R. Goldstein, A. Miranville, G. Schimperna, A Cahn-Hilliard model in a domain with non-permeable walls, Phys. D, Nonlinear Phenom. 240 (2011) 754–766.
[10] R. Kenzler, F. Eurich, P. Maass, B. Rinn, J. Schropp, E. Bohl, W. Dieterich, Phase separation in confined geometries: solving the Cahn-Hilliard equation with generic boundary conditions, Comput. Phys. Commun. 133 (2001) 139–157.
[11] C. Liu, H. Wu, An energetic variational approach for the Cahn–Hilliard equation with dynamic boundary condition: model derivation and mathematical analysis, Arch. Ration. Mech. Anal. 233 (2019) 167–247.
[12] R. Chill, E. Fašangová, J. Prüss, Convergence to steady states of solutions of the Cahn-Hilliard and Caginalp equations with dynamic boundary conditions, Math. Nachr. 279 (2006) 1448–1462.
[13] C.G. Gal, A Cahn–Hilliard model in bounded domains with permeable walls, Math. Methods Appl. Sci. 29 (2006) 2009–2036.
[14] C.G. Gal, Exponential attractors for a Cahn-Hilliard model in bounded domains with permeable walls, Electron. J. Differ. Equ. 143 (2006) 1–23.
[15] G. Gilardi, A. Miranville, G. Schimperna, On the Cahn-Hilliard equation with irregular potentials and dynamic boundary conditions, Commun. Pure Appl. Anal. 8 (2009) 881.
[16] H. Israel, Long time behavior of an Allen-Cahn type equation with a singular potential and dynamic boundary conditions, J. Appl. Anal. Comput. 2 (2012) 29–56.
[17] H.P. Fischer, P. Maass, W. Dieterich, Novel surface modes in spinodal decomposition, Phys. Rev. Lett. 79 (1997) 893.
[18] H.P. Fischer, P. Maass, W. Dieterich, Diverging time and length scales of spinodal decomposition modes in thin films, Europhys. Lett. 42 (1998) 49.
[19] H. Israel, A. Miranville, M. Petcu, Numerical analysis of a Cahn–Hilliard type equation with dynamic boundary conditions, Ric. Mat. 64 (2015) 25–50.
[20] F. Nabet, Finite-volume analysis for the Cahn-Hilliard equation with dynamic boundary conditions, in: Finite Volumes for Complex Applications VII-Methods and Theoretical Aspects, Springer, 2014, pp. 401–409.
[21] N. Li, P. Lin, F. Gao, Energy law preserving finite element scheme for the Cahn-Hilliard equations with dynamic boundary conditions, Commun. Comput. Phys. 26 (2019) 1490–1509.
[22] S. Metzger, An efficient and convergent finite element scheme for Cahn-Hilliard equations with dynamic boundary conditions, SIAM J. Numer. Anal. 59 (2021) 219–248.
[23] X. Bao, H. Zhang, Numerical approximations and error analysis of the Cahn-Hilliard equation with dynamic boundary conditions, Commun. Math. Sci. 19 (2021) 663–685.
[24] J. Shen, X. Yang, Numerical approximations of Allen-Cahn and Cahn-Hilliard equations, Discrete Contin. Dyn. Syst. 28 (2010) 1669.
[25] J. Shen, J. Xu, J. Yang, The scalar auxiliary variable (SAV) approach for gradient flows, J. Comput. Phys. 353 (2018) 407–416.
[26] Q. Cheng, J. Shen, Multiple scalar auxiliary variable (MSAV) approach and its application to the phase-field vesicle membrane model, SIAM J. Sci. Comput. 40 (2018) A3982–A4006.
[27] J. Shen, Efficient spectral-Galerkin method I. Direct solvers for second- and fourth-order equations by using Legendre polynomials, SIAM J. Sci. Comput. 15 (1994) 1489–1505.

[28] F. Chen, J. Shen, Efficient spectral-Galerkin methods for systems of coupled second-order equations and their applications, J. Comput. Phys. 231 (2012) 5016–5028.
[29] M.A. Woodbury, Inverting modified matrices, in: Statistical Research Group, in: Memo. Rep., vol. 42, Princeton University, Princeton, NJ, 1950.
[30] R.E. Lynch, J. Rice, D.H. Thomas, Direct solution of partial difference equations by tensor product methods, Numer. Math. 6 (1964) 185–199.
[31] D.B. Haidvogel, T. Zang, The accurate solution of Poisson's equation by expansion in Chebyshev polynomials, J. Comput. Phys. 30 (1979) 167–180.
[32] J. Shen, Efficient Chebyshev-Legendre Galerkin methods for elliptic problems, in: Proceedings of ICOSAHOM, vol. 95, Citeseer, 1996, pp. 233–239.
[33] J. Lopez, F. Marques, J. Shen, An efficient spectral-projection method for the Navier–Stokes equations in cylindrical geometries: II. Three-dimensional cases, J. Comput. Phys. 176 (2002) 384–401.
[34] P. Knopf, K.F. Lam, C. Liu, S. Metzger, Phase-field dynamics with transfer of materials: the Cahn-Hilliard equation with reaction rate dependent dynamic boundary conditions, ESAIM: Math. Model. Numer. Anal. 55 (2021) 229–282.
[35] X. Bao, H. Zhang, Numerical approximations and error analysis of the Cahn-Hilliard equation with reaction rate dependent dynamic boundary conditions, J. Sci. Comput. 87 (2021) 1–32.
[36] X. Meng, X. Bao, Z. Zhang, Second order stabilized semi-implicit scheme for the Cahn-Hilliard model with dynamic boundary conditions, arXiv preprint, arXiv:2206.07325, 2022.
[37] S. Metzger, A convergent sav scheme for Cahn-Hilliard equations with dynamic boundary conditions, arXiv preprint, arXiv:2203.12326, 2022.